



Bifunctional Fenton-like catalyst enabling oxidative and reductive removal of contaminants synergically in chemical reagent-free aerated solution

Chuhyung Kim ^a, Soonhyun Kim ^b, Yiseul Park ^{c,*}, Wonyong Choi ^{a,*}

^a KENTECH Institute for Environmental and Climate Technology, Korea Institute of Energy Technology (KENTECH), Naju 58330, Republic of Korea

^b Smart Textile Convergence Research Group, Daegu Gyeongbuk Institute of Science and Technology (DGIST), Daegu 42988, Republic of Korea

^c Department of Chemical Engineering, Pukyong National University, Busan 48513, Republic of Korea



ARTICLE INFO

Keywords:

Iron oxide catalyst
Carbon nanofiber
Redox conversion of water contaminants
Reactive oxygen species generation
Catalysis for water treatment

ABSTRACT

This study demonstrated the performance of Fe_2O_3 nanorods-loaded carbon nanofiber sheet ($\text{Fe}_2\text{O}_3/\text{CNF}$) as a heterogeneous Fenton-like catalyst for simultaneous removal of various organic and inorganic contaminants without external energy input and chemical reagents. $\text{Fe}_2\text{O}_3/\text{CNF}$ exhibited notable activities for spontaneous oxidative degradation and reductive transformation in ambient solution, with a synergistic effect for removing dual contaminants (organic||inorganic). The synergistic redox conversions on $\text{Fe}_2\text{O}_3/\text{CNF}$ were facilitated by the *in-situ* generation of oxidant and reductant. The additional oxidant can be generated by the reaction of chromium species with *in-situ* produced H_2O_2 while the additional reductant can be generated by the incomplete oxidation of organic contaminants. Various spectroscopic characterizations and mechanistic analyses suggest that simultaneous redox conversions are induced by spontaneous electron transfers on $\text{Fe}_2\text{O}_3/\text{CNF}$. Furthermore, a flow-reactor equipped with $\text{Fe}_2\text{O}_3/\text{CNF}$ achieved the simultaneous removal of dual contaminants, making it an effective reactive filter that operates without chemical reagents for water treatment.

1. Introduction

Iron oxide, being one of the most abundant and cheap oxide materials, is widely used as a catalyst for oxidation (particularly the Fenton reaction [1]) and reduction reactions in environmental remediation processes. The Fenton reaction can be further enhanced by the supply of additional energy such as light and electricity and can be classified as photo-Fenton [2–4], electro-Fenton [5–8], or photoelectro-Fenton reaction [9–12] depending on the external energy source. These Fenton systems need H_2O_2 and ferrous ions (Fe^{2+}) or *in-situ* generation of H_2O_2 through O_2 reduction with the subsequent decomposition of H_2O_2 by Fenton catalysts to generate highly reactive $\cdot\text{OH}$ for the degradation of organic pollutants [13]. The Fenton reactions can be boosted in various ways. For example, the amidoxime chelated ferrous iron catalyst (U-g-PAO/Fe) effectively enhanced the Fenton activity under light irradiation [3]. U-g-PAO/Fe catalyst has a strong visible light absorbance which promotes the cycling of Fe(II) and Fe(III) and subsequently improves the degradation efficiency up to ~100%. Fe, N-doped biochar material served as a cathodic catalyst for heterogeneous electro-Fenton degradation of sulfadiazine [5]. The electrochemically *in-situ* generated H_2O_2 via oxygen reduction reaction (ORR) was immediately

decomposed by the Fe species in the material. In a photoelectrochemical system that needs the input of both light and electricity, the degradation of organic contaminants was significantly enhanced using $\text{Fe}_3\text{O}_4@-\text{SiO}_2@$ mesoporous TiO_2 photoelectrode in the presence of H_2O_2 [12]. However, most of the previous studies on the iron-based oxidative degradation processes required an excess amount of chemical oxidants and/or external energy input to initiate the reactions, which increases the operating cost.

On the other hand, the iron oxide-based reductive transformation of inorganic contaminants has been much less studied while its oxidative counterpart has been frequently investigated. Typically, adsorption or reductive transformations of inorganic contaminants rely on various approaches employing iron oxide heterojunction with carbon nanomaterials [14–17] or zero-valent iron (ZVI, Fe^0) [18–24]. The combination of iron oxide with carbon nanomaterials has shown promising results in terms of adsorption-reduction activity. For example, the oxygen-containing functional groups on the carbon nanomaterials serve as efficient adsorption sites [14,16], while the functional groups on humic acid (HA) may act as ligands leading to the reductive transformation of Cr(VI) to Cr(III) [17]. Similarly, ZVI has often been used for the reductive removal of multivalent heavy metal ions. Fe^0 , which is an

* Corresponding authors.

E-mail addresses: dewpark@pknu.ac.kr (Y. Park), wchoi@kentech.ac.kr (W. Choi).

intrinsic electron donor [18,19], can adsorb heavy metals on the core-shell structure of nZVI, followed by the gradual reduction of adsorbed heavy metals by Fe^{2+} dissolved from nZVI [19,25]. Similarly, core-shell $\text{Fe@Fe}_2\text{O}_3$ nanowires induce Cr(VI) reduction via electrons transferred from the iron core [24]. However, iron-based reduction technologies, including combination with carbon nanomaterials and ZVI usually require an anoxic (dissolved O_2 -free) condition for effective reductive transformation of inorganic contaminants [15,26–28], which limits the practical applications.

Most of the iron-based redox transformation studies have employed a single substrate as a test compound in widely varying experimental conditions. The iron-based redox conversion systems that demonstrate the simultaneous oxidative and reductive conversions of multiple contaminants are few. Ideally, the iron-based remediation system needs a multi-functional environmental catalytic material that should work in ambient air-equilibrated conditions without additional energy inputs and chemical reagents. Despite extensive investigations into iron oxide-based environmental remediation technologies, the successful cases are limited. Herein, we introduce a novel heterogeneous Fenton-like catalyst of $\text{Fe}_2\text{O}_3/\text{CNF}$ (carbon nanofiber) nanocomposite, which facilitates simultaneous and synergistic redox conversions under ambient aerated conditions without any additional inputs of energy and chemical reagents. Our recent studies have demonstrated that the heterojunction nanocomposite of $\text{Fe}_2\text{O}_3/\text{CNF}$ exhibits abnormal spontaneous reactivity under ambient aerated conditions [29,30]. For instance, $\text{Fe}_2\text{O}_3/\text{CNF}$ exhibited selective degradation of aromatic compounds under ambient aerated conditions without additional chemical oxidants [30]. It was proposed that the interfacial contact between Fe_2O_3 and CNF facilitates the spontaneous electron transfer from aromatic compounds to Fe_2O_3 , which subsequently transfers the electrons to dissolved O_2 to generate reactive oxygen species (ROS). $\text{Fe}_2\text{O}_3/\text{CNF}$ could reductively transform a variety of inorganic substrates as well even in the presence of dissolved O_2 without chemical reductants [29]. It was proposed that the spontaneous electron transfer from the oxygen-containing functional groups (C-OH) on CNF to Fe_2O_3 NRs initiates the reductive transformation of inorganic substrates on $\text{Fe}_2\text{O}_3/\text{CNF}$. In this study, we newly demonstrate the synergistic effect of the simultaneous redox conversions of multiple contaminants on $\text{Fe}_2\text{O}_3/\text{CNF}$. In particular, a cascade redox cycle generated a series of additional oxidants and reductants to facilitate synergistic redox conversions on $\text{Fe}_2\text{O}_3/\text{CNF}$. The simultaneous redox conversions were systematically investigated to understand its overall conversion mechanism. Furthermore, we developed the $\text{Fe}_2\text{O}_3/\text{CNF}$ -based *point-of-use* device for water treatment and demonstrated its successful application as a reactive filter that can remove low-level aqueous contaminants without needing external energy and chemical inputs.

2. Experimental details

2.1. Chemical reagents

The following chemicals were purchased and used as received: The chemicals that were used as-received in this study include the following: Polyacrylonitrile (PAN, $M_w = 150,000$, Aldrich), N,N-dimethylformamide (99%, SAMCHUN Chemicals), hydrogen peroxide (H_2O_2 , 30 wt.%, Junsei), iron (II) sulfate heptahydrate ($\text{FeSO}_4 \cdot 7\text{H}_2\text{O}$, Aldrich), ferric hydroxide oxide (FeOOH , Aldrich), iron (III) oxide (Fe_2O_3 , Aldrich), iron (II, III) oxide (Fe_3O_4 , Aldrich), 4-chlorophenol (4-CP, Aldrich), 4-chlorocatechol (4-CC, Aldrich), hydroquinone (HQ, Aldrich), catechol (CC, Aldrich), *p*-benzoquinone (*p*-BQ, Aldrich), hydroxyhydroquinone (HHQ, Aldrich), sodium chromate dihydrate ($\text{Na}_2\text{CrO}_4 \cdot 2\text{H}_2\text{O}$, Aldrich), 4-nitrophenol (4-NP, Aldrich), acetaminophen (AP, Aldrich), carbamazepine (CBZ, Aldrich), benzoic acid (BA, Aldrich), sodium iodate (NaIO_3 , Aldrich), potassium peroxymonosulfate (OXONE, HSO_5^- , Aldrich), potassium persulfate ($\text{S}_2\text{O}_8^{2-}$, Aldrich), sodium bromate (NaBrO_3 , Aldrich), sodium selenite (Na_2SeO_3 , Aldrich),

terephthalic acid (TA, Aldrich), iron (III) chloride hexahydrate ($\text{FeCl}_3 \cdot 6\text{H}_2\text{O}$, Aldrich), hydrochloric acid (HCl, 37%, Aldrich), sodium nitrate (NaNO_3 , Aldrich), sodium borohydride (NaBH_4 , Junsei), L-ascorbic acid (AA, Aldrich), phosphate monobasic (NaH_2PO_4 , Aldrich), sodium phosphate dibasic (Na_2HPO_4 , Aldrich), 1,5-diphenylcarbazide (DPC, Aldrich), sodium bicarbonate (NaHCO_3 , Kanto Chemical), sodium carbonate (Na_2CO_3 , Junsei), potassium biphenylate ($\text{C}_8\text{H}_5\text{KO}_4$, Alfa Aesar), potassium iodide (KI, Aldrich), sodium hydroxide (NaOH, Aldrich), ammonium molybdate ($(\text{NH}_4)_2\text{MoO}_4$, Aldrich), phosphoric acid (H_3PO_4 , Aldrich), and acetonitrile (CH_3CN , J.T. Baker), *tert*-butanol (TBA, Aldrich), superoxide dismutase from bovine erythrocytes (SOD, Aldrich), 5,5-dimethyl-1-pyrroline-N-oxide (DMPO, Aldrich).

2.2. Preparation of $\text{Fe}_2\text{O}_3/\text{CNF}$

Sheet-like nanocomposites of carbon nanofiber (CNF) and iron oxide-loaded CNF ($\text{Fe}_2\text{O}_3/\text{CNF}$) were fabricated by previously reported methods [30,31]. CNF prepared by the electrospinning technique was used as a substrate for the electrodeposition of FeOOH . FeOOH was deposited on the CNF immersed in an aqueous solution of 0.1 M FeSO_4 by anodic electrodeposition at +1.2 V (vs. Ag/AgCl) and 70 °C until 500 C of charge had passed through 1 g of CNF (500 C g⁻¹). The FeOOH/CNF composite was then converted into the $\text{Fe}_2\text{O}_3/\text{CNF}$ composite by annealing at 400 °C for 4 h in air. Another control material, iron oxide NRs-loaded FTO (denoted as $\text{Fe}_2\text{O}_3/\text{FTO}$), was synthesized by following the previous hydrothermal method [32]. The FTO was vertically aligned in a Teflon tube containing $\text{FeCl}_3 \cdot 6\text{H}_2\text{O}$ and NaNO_3 . The solution was acidified by HCl to prevent precipitation. The Teflon tube was then placed in a stainless-steel reactor, kept in an oven at 100 °C for 6 h, and cooled to room temperature. Then, FeOOH/FTO was rinsed with deionized water, dried at room temperature, and annealed at 550 °C for 1 h and at 800 °C for 20 min to convert it to $\text{Fe}_2\text{O}_3/\text{FTO}$.

2.3. Experimental procedure

All test reactions were carried out in a Pyrex reactor (20 mL) under ambient air-equilibrated conditions. Aliquots of the stock solution of target substrates were added to deionized water to make the desired concentration of the target substrate (typically, 20 μM and 40 μM for the organic and inorganic substrate, respectively). Sample aliquots were withdrawn from the reactor at predetermined time intervals for analyses. The dissolved gas was controlled by purging the Pyrex reactor with a continuous gas (O_2 or Ar) flow for 1 h, and then the calculated amount of the target substrate was spiked into the reactor to start the reaction immediately.

2.4. Continuous flow test

Various simultaneous redox conversions of the coupled organic & inorganic substrates (*i.e.*, 4-CP|| CrO_4^{2-} , AP|| SeO_3^{2-} , BA|| BrO_3^- , where the concentration of target organic and inorganic contaminants were 10 μM and 20 μM , respectively) were carried out in a flow reactor cell with a pump (Flow cell: CP20, Gauss Union; Peristaltic pump: BT50s-1-CE-W, Leadfluid). The nanocomposite of $\text{Fe}_2\text{O}_3/\text{CNF}$ (working area = 2 x 2 cm²) was placed in the center of the reactor and then the target substrate solution continuously flowed through the reactor for 24 h. The flow rate was 6.3 mL min⁻¹, and the total reaction volume was 100 mL.

2.5. Analytical methods

The residual concentration of organic contaminants (*i.e.*, 4-CP, 4-NP, AP, CBZ, and BA) was measured by using a high-performance liquid chromatograph (HPLC, Agilent 1260 Infinity) equipped with a diode array detector and a ZORBAX 300SB-C18 column (4.6 mm x 150 mm). A binary mixture consisting of 0.1% aqueous phosphoric acid and acetonitrile (70:30 v/v) was used as a mobile phase. The removal of the

total organic carbon (TOC) was monitored by using a TOC analyzer (Shimadzu TOC-V_{SH}). The concentration of Cl^- , IO_3^- , and BrO_3^- was quantified with an ion chromatograph (IC, Dionex DX-120) equipped with a Dionex Ionpac AS-14 column and a conductivity detector. The eluent comprised of 3.5 mM Na_2CO_3 and 1 mM NaHCO_3 . The residual concentration of Cr(VI) was quantified using a colorimetric method employing 1,5-diphenylcarbazide (DPC) as a reagent. Absorbance measurements at 540 nm were done using a UV-visible spectrophotometer (Libra S22, Biochrom). The concentration of SeO_3^{2-} was also determined colorimetrically (by measuring absorbance at 500 nm) employing AA and HCl as reagents [33]. The concentration of persulfates (*i.e.*, HSO_5^- and $\text{S}_2\text{O}_8^{2-}$) was quantified based on the spectrophotometric determination of iodine ($\lambda = 352$ nm) formed *via* the reaction of persulfates and iodide [34]. The *in-situ* produced H_2O_2 was quantified using the iodometric titration method [35]. A sample aliquot of treated water was mixed with both biphenylate and iodide solutions and stirred vigorously for 2 min before measuring its absorbance ($\lambda = 372$ nm). After completing the redox conversions, the concentration of the dissolved iron species was determined using Inductively Coupled Plasma optical emission spectrometry (ICP-OES-6300, Thermo Scientific). For electron paramagnetic resonance (EPR) analyses, DMPO was employed as a spin-trapping reagent for $\cdot\text{OH}$ and O_2^- . The EPR spectra were obtained using a JEOL JES-X310 spectrometer at the following conditions: center field = 335 mT; microwave frequency = 9.415 GHz; microwave power = 1.00 mW; modulation frequency = 100 kHz; and modulation width = 0.2 mT.

2.6. Material characterizations

The surface morphology images of bare CNF and $\text{Fe}_2\text{O}_3/\text{CNF}$ were obtained using a field emission scanning electron microscope (FE-SEM-II, JSM 7800 F). X-ray diffraction patterns measurement of each sample was conducted using a PANalytical X'pert diffractometer (Cu-K α radiation) with an X'Celerator detector. All X-ray photoelectron spectroscopy (XPS, VG Escalab 250) analyses were performed using a monochromatic Al-K α line (1486.6 eV) as an excitation source at the KBSI Busan center. All XPS spectra were calibrated with respect to the C 1 s peak (284.6 eV).

The surface oxygen-containing functional groups on $\text{Fe}_2\text{O}_3/\text{CNF}$ were detected by attenuated total reflectance Fourier transform infrared spectroscopy (ATR-FT-IR, Thermo Scientific, iS50) using ZnSe crystals. The Raman spectra were monitored using a LabRam ARAMIS Raman spectrometer (Horiba Jobin-Yvon) with Ar-ion laser excitation at 514 nm. All X-ray absorption near-edge structure (XANES) experiments were conducted at the 8C nano XAFS beamline of Pohang Light Source-II.

2.7. Electrochemical measurements

The spontaneous electron transfer occurring on the $\text{Fe}_2\text{O}_3/\text{CNF}$ (or bare CNF) electrode upon adding the reducible (Cr(VI)) or the oxidizable substrate (4-CP) was monitored by measuring the current generation in an electrochemical cell consisting of the $\text{Fe}_2\text{O}_3/\text{CNF}$, Pt wire, and Ag/AgCl (3 M KCl) as a working, counter, and reference electrode, respectively. A potentiostat (Gamry Instruments Reference 600) was used for the electrochemical measurement. A phosphate buffer solution (PBS, 0.1 M, 30 mL) was used as an electrolyte. Before the addition of contaminants (4-CP and Cr(VI)), the open-circuit potential (V_{oc}) of $\text{Fe}_2\text{O}_3/\text{CNF}$ was monitored until it reached stabilization. The stabilized V_{oc} was applied for collecting the current while spiking an aliquot of the contaminants.

3. Results and discussions

3.1. Physicochemical characterizations of $\text{Fe}_2\text{O}_3/\text{CNF}$

The morphologies of bare CNF and $\text{Fe}_2\text{O}_3/\text{CNF}$ were monitored by SEM images as shown in Fig. 1a and b. The smooth surface of bare CNF was found to be uniformly covered with Fe_2O_3 NRs, which had a diameter of ~ 10 nm and an average length of ~ 150 nm [30]. The XRD patterns of bare CNF and $\text{Fe}_2\text{O}_3/\text{CNF}$ are compared as shown in Fig. 1c. The broad peak centered at 25° corresponds to the graphitic (002) peak which is characteristic of many carbon products [36]. The XRD peak in the $\text{Fe}_2\text{O}_3/\text{CNF}$ sample matches well with the standard $\alpha\text{-Fe}_2\text{O}_3$ (JCPDS card No. 33-0664) [31]. However, a small FeOOH peak (JCPDS card No. 1-0662) remained on the $\text{Fe}_2\text{O}_3/\text{CNF}$ sample due to the insufficient

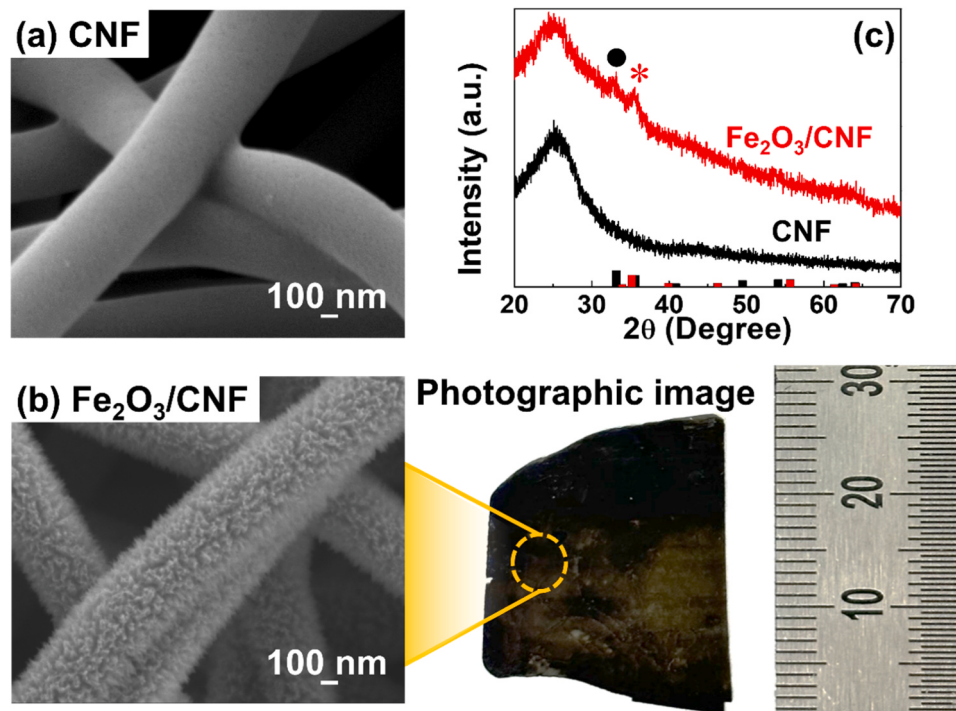


Fig. 1. SEM images of (a) bare CNF, (b) $\text{Fe}_2\text{O}_3/\text{CNF}$, (c) XRD patterns of bare CNF and $\text{Fe}_2\text{O}_3/\text{CNF}$ (*: Fe_2O_3 (red bar), •: FeOOH (black bar)).

calcination temperature, which was necessary to prevent the CNF sheet from being oxidized to CO_2 . The XPS Fe 2p spectra of $\text{Fe}_2\text{O}_3/\text{CNF}$ and commercial Fe_2O_3 nanoparticles are compared in Fig. S1a. The binding energy (B.E.) of the Fe 2p_{3/2} peak of $\text{Fe}_2\text{O}_3/\text{CNF}$ is 710.98 eV, slightly shifted compared to that of the reference Fe_2O_3 sample (710.58 eV). This difference is attributed to the different preparation methods of Fe_2O_3 and the presence of FeOOH fraction that remains in $\text{Fe}_2\text{O}_3/\text{CNF}$. Furthermore, the O 1 s XPS spectra exhibited a clear difference between the Fe_2O_3 nanoparticle and $\text{Fe}_2\text{O}_3/\text{CNF}$ (see Fig. S1b). A peak at 529.88 eV was observed for both Fe_2O_3 and $\text{Fe}_2\text{O}_3/\text{CNF}$, which is assigned as the lattice oxygen species of Fe_2O_3 . The additional two peaks at 531.48 eV and 532.48 eV were observed on $\text{Fe}_2\text{O}_3/\text{CNF}$ and bare CNF, respectively, and were assigned as the surface OH groups on Fe_2O_3 and CNF [29, 37–39].

3.2. Simultaneous and synergistic redox conversions on $\text{Fe}_2\text{O}_3/\text{CNF}$

The simultaneous redox conversions of various contaminants couples on bare CNF and $\text{Fe}_2\text{O}_3/\text{CNF}$ are compared in Fig. 2a. Compared with the removal of the single substrate alone, $\text{Fe}_2\text{O}_3/\text{CNF}$ exhibited a

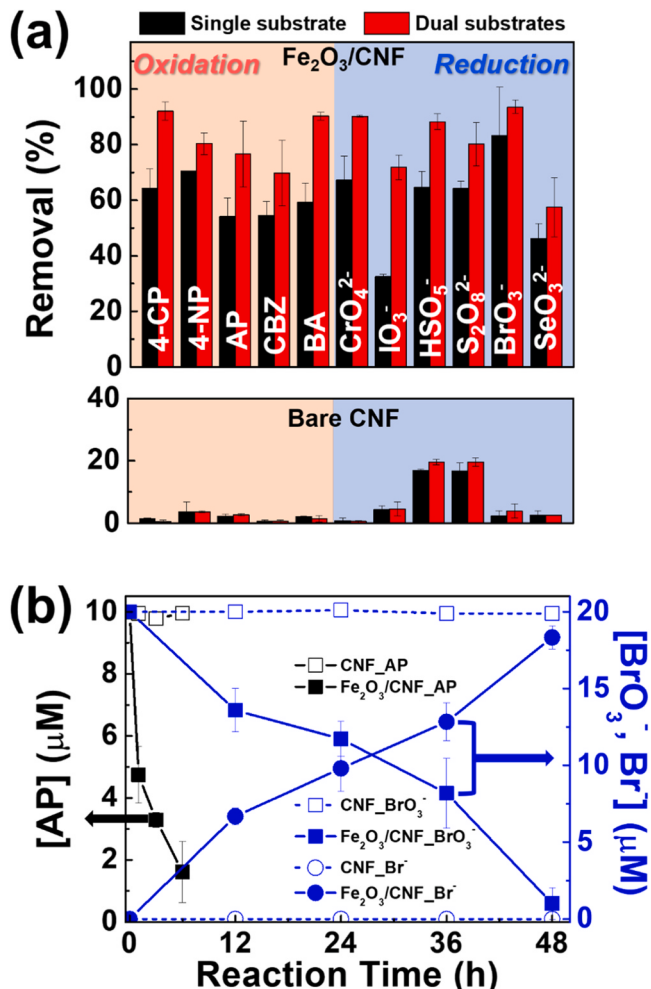
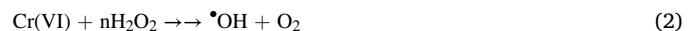
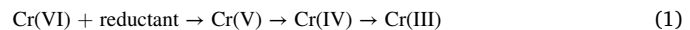


Fig. 2. (a) The removal efficiencies of the target substrate (organic or inorganic) that is present alone (as the single substrate) or co-present with the counterpart substrate (as the dual substrates: e.g., CrO_4^{2-} with an organic substrate, 4-CP with an inorganic substrate) in bare CNF and $\text{Fe}_2\text{O}_3/\text{CNF}$ systems under ambient aerated condition (reaction time: 6 h). (b) Time profiles of the simultaneous removal of aqueous contaminants couple: AP|| BrO_3^- couple on $\text{Fe}_2\text{O}_3/\text{CNF}$ under ambient aerated condition. $[\text{Sample}] = 2 \text{ g L}^{-1}$, $[\text{4-CP, 4-NP, AP, CBZ, and BA}]_0 = 20 \mu\text{M}$, and $[\text{CrO}_4^{2-}, \text{IO}_3^-, \text{HSO}_5^-, \text{S}_2\text{O}_8^{2-}, \text{and } \text{BrO}_3^-]_0 = 40 \mu\text{M}$. For Fig. 2b, $[\text{AP}]_0 = 10 \mu\text{M}$, and $[\text{BrO}_3^-]_0 = 20 \mu\text{M}$.

significant synergistic effect on the simultaneous redox removals of various contaminants couples (i.e., 4-CP, 4-NP, AP, CBZ, and BA in the presence of Cr(VI)), as well as various inorganic contaminants (i.e., CrO_4^{2-} , IO_3^- , HSO_5^- , $\text{S}_2\text{O}_8^{2-}$, BrO_3^- , and SeO_3^{2-} in the presence of 4-CP). It is worth noting that the simultaneous redox conversion efficiencies varied for various target contaminant couples, but all exhibited a synergistic effect with $\text{Fe}_2\text{O}_3/\text{CNF}$. To further confirm the outstanding simultaneous redox conversions on $\text{Fe}_2\text{O}_3/\text{CNF}$, the removal of AP and BrO_3^- couple was monitored along with the concurrent generation of Br^- as shown in Fig. 2b. AP and BrO_3^- were simultaneously removed by $\text{Fe}_2\text{O}_3/\text{CNF}$, whereas bare CNF was completely inactive. Furthermore, $\text{Fe}_2\text{O}_3/\text{CNF}$ quantitatively converted BrO_3^- to Br^- , which confirms that BrO_3^- is removed via a reductive mechanism, not simple adsorption.

To elucidate the simultaneous and synergistic redox conversion activities on $\text{Fe}_2\text{O}_3/\text{CNF}$, we selected 4-CP and Cr(VI) as the target contaminants couple as shown in Fig. 3a and b. The simultaneous redox conversions on $\text{Fe}_2\text{O}_3/\text{CNF}$ were compared with bare CNF, commercial iron oxide nanoparticles (NPs) (i.e., FeOOH , Fe_2O_3 , and Fe_3O_4), a physical mixture of both (denoted as $\text{Fe}_2\text{O}_3 + \text{CNF}$), and $\text{Fe}_2\text{O}_3/\text{FTO}$ under the same reaction conditions as shown in Fig. 3a, b, and S2. Among those materials, bare CNF, commercial iron oxide NPs, and $\text{Fe}_2\text{O}_3/\text{FTO}$ exhibit negligible reaction activities, whereas $\text{Fe}_2\text{O}_3/\text{CNF}$ only exhibits a marked synergistic effect on the simultaneous redox conversions. It should be noted that the ambient reaction of $\text{Fe}_2\text{O}_3/\text{CNF}$ in an aerated solution accompanied the *in-situ* production of H_2O_2 as shown in Fig. 3c. Bare CNF and Fe_2O_3 NP exhibited negligible H_2O_2 production, which is consistent with their negligible simultaneous redox activities (see Fig. 3a, b, and S2). $\text{Fe}_2\text{O}_3/\text{CNF}$ showed negligible H_2O_2 production under the Ar-purged condition, which indicates that the *in-situ* H_2O_2 is generated from the reduction reaction of dissolved O_2 . It should be also noted that the presence of Cr(VI) lowered the peak production of *in-situ* H_2O_2 under the aerated condition. This implies that Cr species reacts with *in-situ* H_2O_2 . It has been reported that the chromium species of various oxidation states (e.g., Cr(III), Cr(IV), Cr(V), and Cr(VI)) can react with H_2O_2 to generate $\cdot\text{OH}$ [40,41], which further serves as an additional oxidant. This implies that both Cr(VI) and its reduced intermediate species can generate $\cdot\text{OH}$ via reactions 1–3. Incidentally, Cr (VI) can be also reduced by *in-situ* intermediates of oxidized phenolic compounds via reaction 1 [42,43].



As a result of the synergic redox conversion, the successful removal of $\sim 41\%$ of TOC was achieved after 6 h of oxidative reaction, which is consistent with the yield of Cl^- generation (Cl^- yield = 40.6%; see Fig. 3a). Overall, $\text{Fe}_2\text{O}_3/\text{CNF}$ successfully demonstrated the ability to initiate simultaneous and synergistic redox conversions under ambient aerated condition without needing additional energy input and chemical reagents.

3.3. Factors affecting the simultaneous redox conversions

The effects of the dissolved gas (O_2 vs. Ar-purged) were tested for the simultaneous and synergistic redox conversions on $\text{Fe}_2\text{O}_3/\text{CNF}$ as shown in Fig. 4a and b. The bare CNF did not exhibit any activity for 4-CP and Cr(VI) removal under either O_2 -purged or Ar-purged conditions. In marked contrast, $\text{Fe}_2\text{O}_3/\text{CNF}$ showed significantly different reactivities depending on the dissolved gas. Firstly, a notably increased 4-CP removal was observed under the O_2 -saturated condition while 4-CP removal was insignificant in the Ar-purged condition (see Fig. 4a). This can be attributed to the role of O_2 participating in 4-CP oxidation and *in-situ* H_2O_2 production and the following reactions of chromium species with H_2O_2 generating $\cdot\text{OH}$ (reactions 2–3) which should further

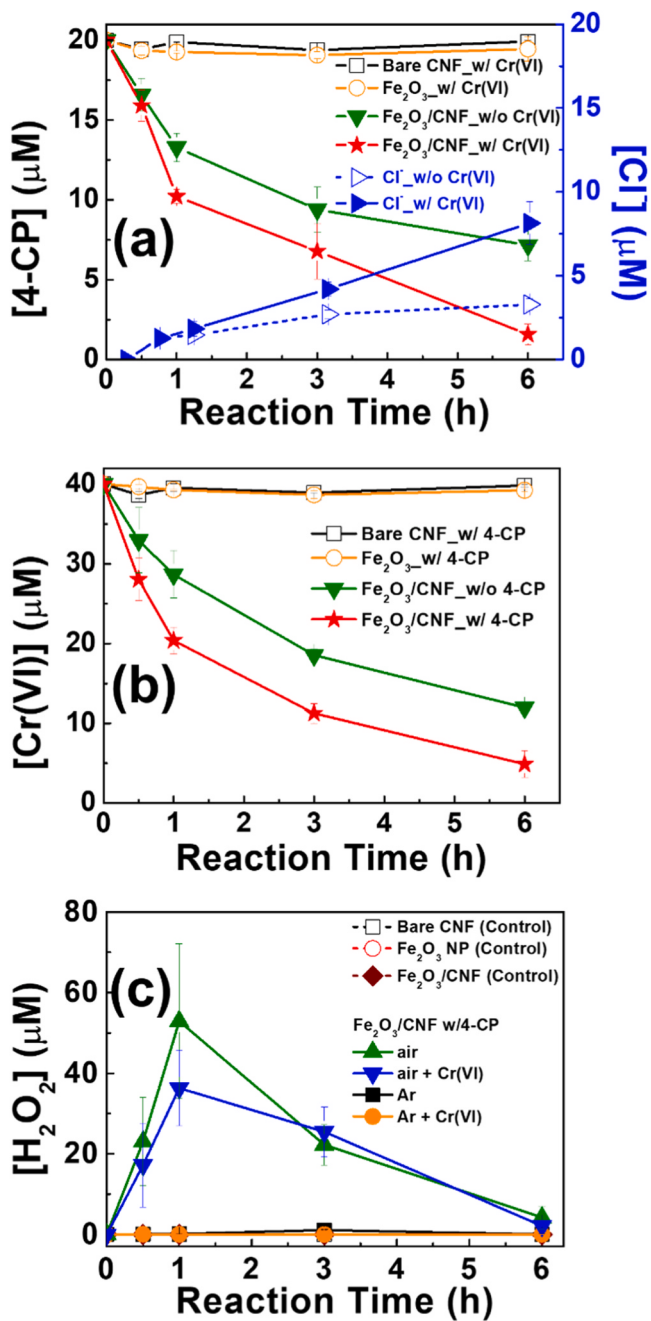


Fig. 3. Simultaneous removal of (a) 4-CP and (b) Cr(VI) as the selected target contaminant on $\text{Fe}_2\text{O}_3/\text{CNF}$ under ambient aerated conditions. [Samples] = 2 g L⁻¹, [4-CP]₀ = 20 μM, and [CrO₄²⁻]₀ = 40 μM. (c) Comparison of *in-situ* H_2O_2 production on $\text{Fe}_2\text{O}_3/\text{CNF}$ under various conditions. The control data for bare CNF, Fe_2O_3 NP, and $\text{Fe}_2\text{O}_3/\text{CNF}$ all overlap with other symbols in the zero level. [Samples] = 2 g L⁻¹, [4-CP]₀ = 20 μM, and [Cr(VI)]₀ = 40 μM.

oxidize 4-CP [30]. On the other hand, the Cr(VI) reduction on $\text{Fe}_2\text{O}_3/\text{CNF}$ was observed under both O_2 -purged and Ar-purged conditions. It has been proposed from our previous study [48] that the spontaneous electron transfer can be initiated from the oxygen-containing functional groups on CNF to reducible inorganic substrates through Fe_2O_3 NRs. In the present case where both oxidizable organic substrate and reducible inorganic substrates are co-present, the removal of Cr(VI) was enhanced in the presence of 4-CP under the O_2 -purged condition as shown in Fig. 4b. This can be attributed to the phenolic intermediates generated during the oxidation of 4-CP under O_2 -purged conditions, which may serve as additional reductants for Cr

(VI) reduction (*via* reaction 1). Thus, the presence of dissolved O_2 is essentially needed for the simultaneous redox conversions on $\text{Fe}_2\text{O}_3/\text{CNF}$.

Several previous studies reported that the Cr(VI) reduction can be induced by the phenolic oxidation intermediates generated from the incomplete oxidation of various phenolic compounds [42,43]. To confirm if the phenolic oxidation intermediates induce the Cr(VI) reduction, the control reactions of several model phenolic intermediates with Cr(VI) were tested in the absence of $\text{Fe}_2\text{O}_3/\text{CNF}$ as shown in Fig. 4c. The model phenolic intermediates such as hydroquinone (HQ), hydroxyhydroquinone (HHQ), catechol (CC), *p*-benzoquinone (*p*-BQ), and 4-chlorocatechol (4-CC) were selected for the Cr(VI) reduction control test. 4-CP alone had negligible activity for Cr(VI) reduction, ruling out its possible role in Cr(VI) reduction. In marked contrast, other phenolic intermediates showed significant activity in Cr(VI) reduction, with HHQ being particularly effective in achieving complete Cr(VI) removal. These findings support the hypothesis that phenolic intermediates generated from the 4-CP oxidation can directly reduce Cr (VI). Further evidence of the involvement of the phenolic intermediates in Cr(VI) reduction was obtained from monitoring the generation of HHQ, HQ, and 4-CC from 4-CP oxidation on $\text{Fe}_2\text{O}_3/\text{CNF}$: the generation of these intermediates was detected in the absence of Cr(VI), but was negligible in the presence of Cr(VI) as shown in Fig. 4d. This implies that the *in-situ* generated phenolic oxidation intermediates (e.g., HHQ, HQ, and 4-CC) are rapidly removed by their reaction with Cr(VI) as soon as they are generated. This observation is consistent with the enhanced generation of Cl^- during 4-CP oxidation in the presence of Cr(VI) as the 4-CP oxidation intermediates can be more mineralized (oxidized) by Cr (VI) with producing more chloride ions (see Fig. 3a).

To investigate the role of reactive oxygen species (ROS) during the simultaneous redox conversions on $\text{Fe}_2\text{O}_3/\text{CNF}$, radical quenching experiments were performed as shown in Fig. 5a and b. 4-CP oxidation (during simultaneous redox conversions) was retarded in the presence of radical quenchers (*i.e.*, SOD and TBA), which implies the ROS generation on $\text{Fe}_2\text{O}_3/\text{CNF}$ during the reaction. Similarly, the Cr(VI) reduction (during simultaneous redox conversions) was also hindered by the presence of the quenchers, which indicates that the ROS are also involved in the Cr(VI) reduction. The observation that both 4-CP oxidation and Cr(VI) reduction are retarded by the addition of quenchers (SOD or TBA) implies that the ROS quenchers hinder not only the 4-CP oxidation but also the Cr(VI) reduction *via* suppressing the generation of 4-CP oxidation intermediates (*i.e.*, reductants of Cr(VI)). Thus, Cr(VI) plays a crucial role in the 4-CP oxidation on $\text{Fe}_2\text{O}_3/\text{CNF}$ during simultaneous redox conversions, and vice versa.

The generation of ROS (*i.e.*, O_2^- and $\cdot\text{OH}$) during the simultaneous redox conversions on $\text{Fe}_2\text{O}_3/\text{CNF}$ was indirectly monitored using chemical probes. The selective reaction of TA with $\cdot\text{OH}$ produces 2-hydroxyterephthalic acid (2-HTA), and its generation can be measured by the fluorescence emission ($\lambda_{\text{ex}} = 315$ nm) as shown in Fig. 5c [44]. It compares 2-HTA generation on $\text{Fe}_2\text{O}_3/\text{CNF}$ in the presence and absence of Cr(VI). The 2-HTA production (*i.e.*, $\cdot\text{OH}$ generation) was enhanced in the presence of Cr(VI), which can be ascribed to the additional generation of $\cdot\text{OH}$ *via* the reaction of chromium species with the *in-situ* produced H_2O_2 (reactions 2–3) [40,41]. This result supports that $\cdot\text{OH}$ serves as a main oxidant during simultaneous redox conversions on $\text{Fe}_2\text{O}_3/\text{CNF}$. The generation of ROS was also confirmed by using the EPR spin-trapping technique as shown in Fig. 5d. The typical DMPO- $\cdot\text{OH}$ (•) and DMPO-OOH (•⁺) peaks were observed on $\text{Fe}_2\text{O}_3/\text{CNF}$ in the presence of both 4-CP and Cr(VI), whereas the signals were much lower in the presence of 4-CP only. Moreover, the addition of SOD significantly suppressed EPR signals, which reconfirms that the generation of $\cdot\text{OH}$ is mediated *via* O_2^- (or HO_2^-). In marked contrast, the bare CNF system exhibited negligible EPR signals, which is consistent with its negligible reactivity as shown in Figs. 2b and 3a. All the above results consistently indicate that the ROS generation on $\text{Fe}_2\text{O}_3/\text{CNF}$ is synergically enhanced when dual substrates (organic||inorganic) are co-present (*e.g.*, 4-CP ||Cr

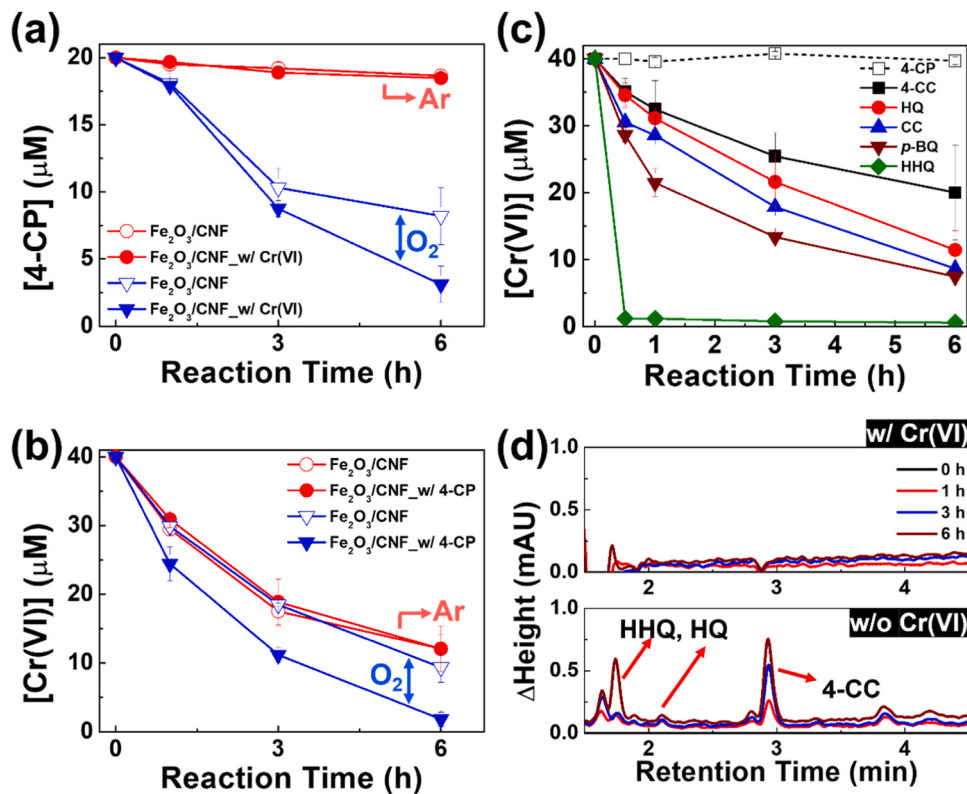


Fig. 4. Gas purging effects on (a) 4-CP oxidation and (b) Cr(VI) reduction on Fe₂O₃/CNF. [Fe₂O₃/CNF] = 2 g L⁻¹, [4-CP]₀ = 20 μM, [Cr(VI)]₀ = 40 μM, and gas was purged for 1 h before the reaction. (c) Control tests of Cr(VI) reduction by externally added model phenolic intermediate in the absence of Fe₂O₃/CNF. [4-CP, 4-CC, HQ, catechol (CC), *p*-benzoquinone (*p*-BQ), and HHQ]₀ = 20 μM, [Cr(VI)]₀ = 40 μM, and air-equilibrated condition. (d) HPLC chromatograms of intermediates generated during a 6 h oxidation reaction of 4-CP on Fe₂O₃/CNF with or without Cr(VI). The Y-axis represents the intensity difference from the initial sample (0 h).

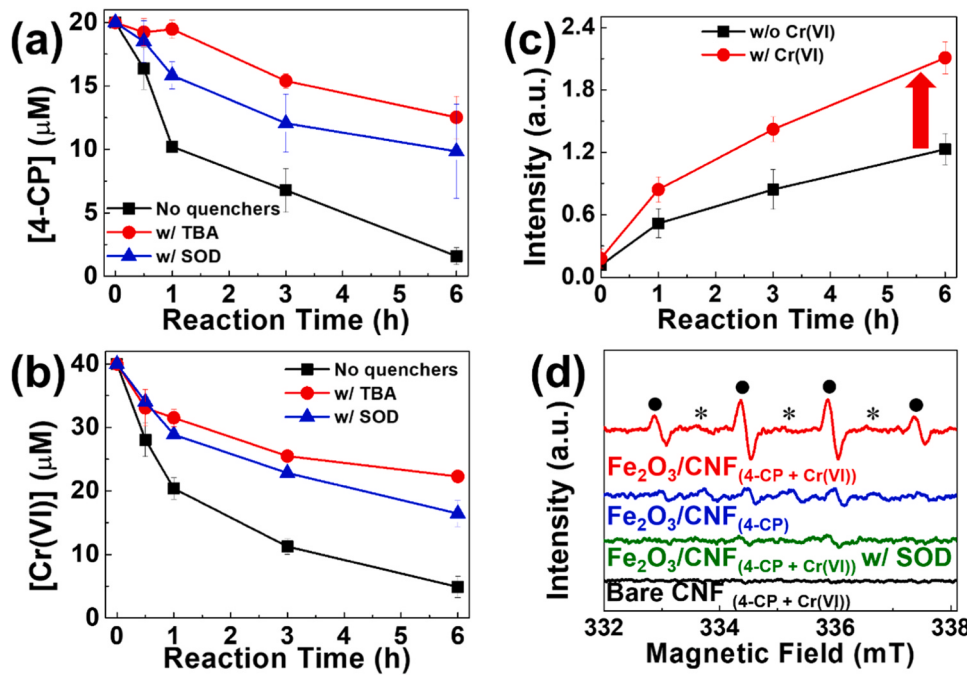


Fig. 5. Radical scavenger effect on (a) 4-CP oxidation and (b) Cr(VI) reduction on Fe₂O₃/CNF under ambient aerated conditions. [Fe₂O₃/CNF] = 2 g L⁻¹, [SOD]₀ = 50 mg L⁻¹, [TBA]₀ = 0.1 M, [4-CP]₀ = 20 μM, and [Cr(VI)]₀ = 40 μM. (c) The time profiles of 2-HTA generation (measured by fluorescence emission intensity) via •OH reaction with TA (as •OH probe reagent) on Fe₂O₃/CNF in the presence or absence of Cr(VI). [Fe₂O₃/CNF] = 2 g L⁻¹, [4-CP]₀ = 20 μM, [Cr(VI)]₀ = 40 μM, and [TA]₀ = 50 μM in 2 mM of NaOH. (d) Spin trap EPR spectra for ROS generation on bare CNF and Fe₂O₃/CNF under various conditions. [Samples] = 5 g L⁻¹, [SOD]₀ = 50 mg L⁻¹, [4-CP]₀ = 20 μM, [Cr(VI)]₀ = 40 μM, and [DMPO] = 50 mM.

(VI), AP || BrO₃).

The simultaneous redox conversions of 4-CP and Cr(VI) were optimized by varying the concentration of each substrate (*i.e.*, 4-CP and Cr (VI)) as shown in Fig. 6a. The result indicates that the optimal concentrations of 4-CP and Cr(VI) are 20 μ M and 40 μ M, respectively. The optimized concentrations should represent the condition where the competitive adsorption of both substrates is compromised on the active redox sites on Fe₂O₃/CNF. When the concentration of the counterpart substrate exceeds an optimal value, the synergistic effect is reduced as the limited active sites are dominantly occupied by the competing counterpart substrates. Therefore, the simultaneous redox conversions of both substrates were significantly hindered in the presence of 1 mM F⁻ that can adsorb on the iron oxide surface as shown in Fig. 6b. On the Fe₂O₃/CNF composite, fluoride ions should be adsorbed mostly on the iron oxide site, not on the hydrophobic CNF surface. In marked contrast, chloride ions that little adsorb on the iron oxide surface had only a minor hindering effect. It is proposed that the presence of fluoride ions hinders the adsorption of 4-CP and Cr(VI) on Fe₂O₃/CNF by substituting the surface hydroxyl groups on Fe₂O₃ ($>\text{Fe-OH} + \text{F}^- \rightarrow >\text{Fe-F} + \text{OH}^-$), thereby retarding the redox conversions on the surface [45, 46]. A similar fluoride inhibition effect on Cr(VI) reduction on Fe₂O₃/CNF was observed while the chloride addition had no effect [29]. This observation also indicates that the active sites on Fe₂O₃/CNF can be

identified as Fe₂O₃ NRs that should be preferably occupied by fluoride ions rather than the CNF surface.

3.4. Mechanistic insights into the simultaneous redox process on Fe₂O₃/CNF

The carbon oxidation state change on Fe₂O₃/CNF was analyzed by XPS before and after the simultaneous redox conversions (see Fig. 7a). The C 1 s XPS spectra indicate that the C-OH peak area was decreased, whereas the C=O and COOH peak areas were markedly increased after the simultaneous redox conversions. A similar trend is shown in the FT-IR and Raman spectra as shown in Fig. 7b and c. The IR peak intensity of C-OH decreased, but that of COOH and C=O increased after the simultaneous redox conversion as shown in Fig. 7b. It has been proposed from the previous study [48] that the electron-rich surface functional groups on CNF (*i.e.*, C-OH) serve as an electron donor to initiate the electron transfer to Cr(VI) (during simultaneous redox conversion). The IR peaks at 1000–1200 cm^{-1} , 1535–1640 cm^{-1} , and 1735 cm^{-1} correspond to C-OH, COOH, and C=O, respectively [47,48]. Furthermore, the ratio of the D and G bands (*i.e.*, I_D/I_G) increased from 0.89 to 1.06 after the simultaneous redox conversions as shown in Fig. 7c. This indicates the increased number of defect sites and oxygen-containing functional groups on the surface of Fe₂O₃/CNF [29,49,50].

XANES analyses confirmed the partially reduced oxidation state of Fe between the fresh and used Fe₂O₃/CNF as shown in Fig. 7d [51,52]. The pre-edge position of the fresh Fe₂O₃/CNF is located at 7114.8 eV, the same energy position as the reference Fe₂O₃ NP. However, the pre-edge position of the used one is shifted to 7114.5 eV, which means that the iron oxide was partially reduced from Fe³⁺ to Fe²⁺. On the other hand, to investigate the Cr(III) formation as a product of the simultaneous redox conversion of 4-CP and Cr(VI), we analyzed Cr 2p XPS spectra (see Fig. 7e). While the appearance of Cr 2p band on the bare CNF after the reaction was negligible, it was clearly identified on Fe₂O₃/CNF, which supported the formation of Cr(III) (576.6 eV and 586.6 eV for Cr 2p_{3/2} and Cr 2p_{1/2}, respectively, the peaks at the 578.5 eV and 589.9 eV are assigned to residual Cr(VI) (Cr 2p_{3/2} and Cr 2p_{1/2}, respectively). This indicates that the removal of Cr(VI) on Fe₂O₃/CNF is caused by the reduction of Cr(VI) to Cr(III), not a simple adsorption.

The electron transfer occurring on Fe₂O₃/CNF can be monitored by an electrochemical measurement using the Fe₂O₃/CNF electrode. The current response was measured upon spiking of 4-CP or Cr(VI) as shown in Fig. 7f. The bare CNF and Fe₂O₃/FTO electrodes exhibited no current change (negligible electron transfer capacity), which is consistent with its negligible reactivity. In marked contrast, the appearance of cathodic current was observed when spiking Cr(VI), whereas an abrupt anodic current was observed upon spiking 4-CP. This electrochemical evidence confirms that 4-CP and Cr(VI) are immediately oxidized and reduced on Fe₂O₃/CNF, respectively whereas bare CNF and Fe₂O₃/FTO induce no electrochemical responses under the same conditions. The redox active sites are generated only when Fe₂O₃ and CNF are directly coupled. To obtain more quantitative information from this electrochemical measurement, the transferred charge during the Cr(VI) spiking was estimated to be about 1207.7 μ C for the initial 30 s, which corresponds to [the average number of electrons transferred on Fe₂O₃/CNF (1.5 cm^2) per second] = $2.5 \times 10^{14}/\text{s}$. If we assume that this electron transfer rate is sustained throughout the reaction, 40 μ M of Cr(VI) (needing 1.44×10^{18} electrons for Cr(VI) to Cr(III) conversion in 20 mL solution) would be removed in 1.6 h. However, it took much longer beyond 6 h (see Fig. 3b), which implies the electron transfer rate should decrease with time. This is consistent with the observation that the cathodic current peak upon spiking Cr(VI) started to decrease at around 45 s in Fig. 7f.

To test the durability of Fe₂O₃/CNF, the simultaneous redox conversions occurring on Fe₂O₃/CNF were repeated up to 10 cycles in the same batch of Fe₂O₃/CNF sample as shown in Fig. 8. As shown in Fig. 8a, 4-CP oxidation activity was gradually decreased due to the accumulation of intermediates on the active sites or partial reduction of Fe³⁺

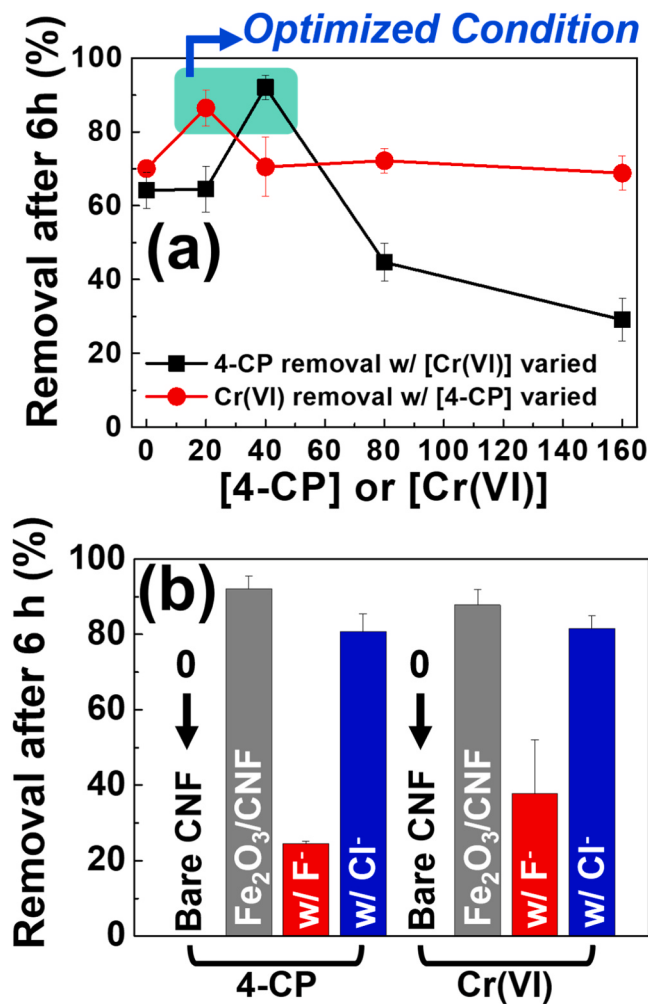


Fig. 6. (a) Contaminant concentration effect on simultaneous removal of 4-CP and Cr(VI). [Fe₂O₃/CNF] = 2 g L⁻¹, and [4-CP]₀ = [Cr(VI)]₀ = 0 ~ 160 μ M. (b) Halide ions (F⁻ and Cl⁻) effect on the simultaneous redox conversions on bare CNF and Fe₂O₃/CNF under ambient aerated conditions. [Samples] = 2 g L⁻¹, [4-CP]₀ = 20 μ M, [Cr(VI)]₀ = 40 μ M, and [NaF]₀ = [NaCl]₀ = 1 mM.

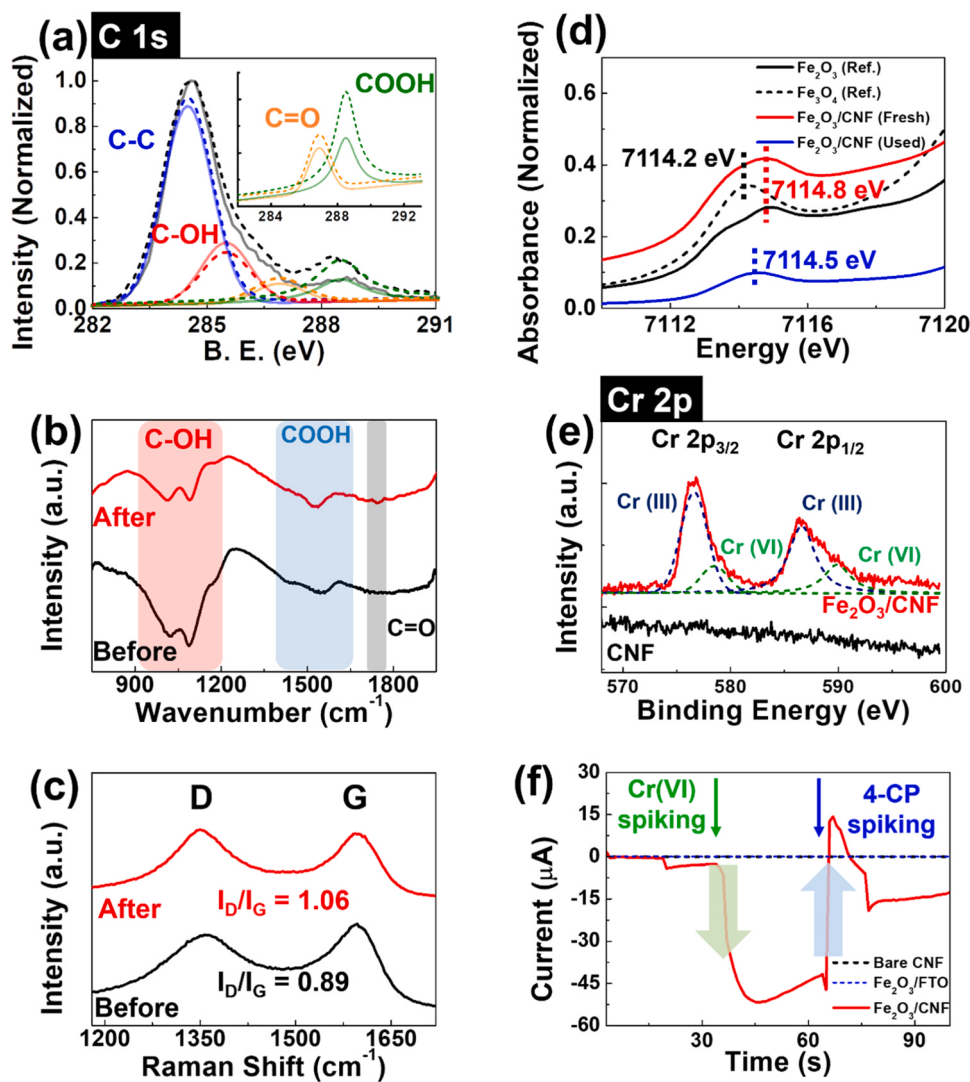


Fig. 7. (a) C 1 s XPS, (b) FT-IR, (c) Raman, (d) XANES, (e) Cr 2p XPS spectra of $\text{Fe}_2\text{O}_3/\text{CNF}$ before and after the simultaneous removal of 4-CP and Cr(VI). The inset in (a) shows the magnified $\text{C}=\text{O}$ and COOH peaks of C 1 s XPS spectra. The solid and dashed lines in C 1 s XPS spectra indicate before and after the redox conversion, respectively. (f) Current changes upon spiking contaminants (i.e., 4-CP and Cr(VI)) onto the bare CNF, $\text{Fe}_2\text{O}_3/\text{FTO}$, and $\text{Fe}_2\text{O}_3/\text{CNF}$ electrode. The red solid line represents the current profile of $\text{Fe}_2\text{O}_3/\text{CNF}$ and the black dashed line does that of bare CNF. $[\text{Phosphate buffer solution}]_0 = 0.1 \text{ M}$, and $[\text{4-CP}]_0 = [\text{Cr (VI)}]_0 = 100 \mu\text{M}$.

during the repetitive reactions [30]. However, in the presence of Cr(VI), the 4-CP oxidation activity was enhanced and the higher activity was maintained through the repeated cycles. A similar behavior was also observed for the repeated cycles of Cr(VI) removal on $\text{Fe}_2\text{O}_3/\text{CNF}$ (see Fig. 8b). The Cr(VI) removal efficiency in the absence of 4-CP was gradually decreased due to the accumulation of Cr(III) on the active sites and the depletion of active surface functional groups on $\text{Fe}_2\text{O}_3/\text{CNF}$ [29]. However, in the presence of 4-CP, Cr(VI) removal efficiency was also highly enhanced, and the higher activity was maintained through the repeated cycles. To monitor the structural change of $\text{Fe}_2\text{O}_3/\text{CNF}$ before and after the repetitive cycles of reaction with 4-CP and Cr(VI), the SEM images of $\text{Fe}_2\text{O}_3/\text{CNF}$ before and after the cycles are compared in Fig. 8c and d, which show that the nanorod structure of Fe_2O_3 is well maintained even after the repetitive reactions. Furthermore, the stability of the iron oxide on $\text{Fe}_2\text{O}_3/\text{CNF}$ was checked by measuring the total dissolved Fe concentration by using ICP-OES after a 6 h reaction, which was estimated to be $\sim 25 \text{ ppb}$. This is negligibly small compared to the total iron content in the $\text{Fe}_2\text{O}_3/\text{CNF}$ nanocomposite sample. This concludes that the $\text{Fe}_2\text{O}_3/\text{CNF}$ sample has a durable composition and a possible role of dissolved iron species in the observed redox conversions

can be ruled out.

Based on the results and discussions, we propose the simultaneous redox conversion mechanism on $\text{Fe}_2\text{O}_3/\text{CNF}$ which is illustrated in Scheme 1. Our previous studies have elucidated the mechanisms of the oxidative and reductive conversion of a single substrate. The oxidative degradation of aromatic compound (AC) initiates through a spontaneous electron transfer from AC to Fe^{3+} on Fe_2O_3 NRs (*via* cation- π interaction), which is then transferred to dissolved O_2 to generate ROS (O_2^\bullet and •OH) (reactions 4–7) [30]. On the other hand, the reductive transformation of inorganic contaminants (IC) is induced by an interfacial potential gradient developed between the Fe_2O_3 NRs and CNF. The oxygen-containing functional group (C-OH) on the surface of CNF serves as an electron donor, and the electron is further transferred to IC through Fe_2O_3 NRs (reactions 8–9) [29]. In the present study, the simultaneous redox conversions of dual substrates can be achieved through the cascade electron transfer from AC to IC through $\text{Fe}_2\text{O}_3/\text{CNF}$. The synergic effect is enabled by coupling the electron donor (AC) and the electron acceptor (IC), which should enhance the overall electron transfer efficiency compared with the case where only a single substrate (either AC or IC alone) is present. The *in-situ* generated intermediates of

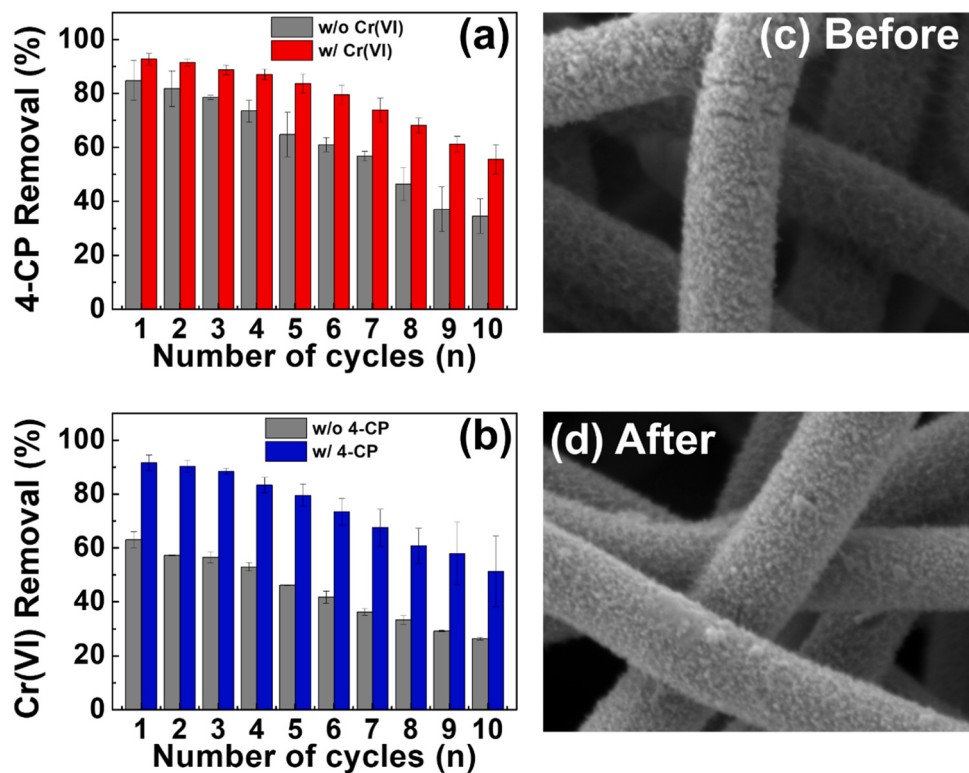
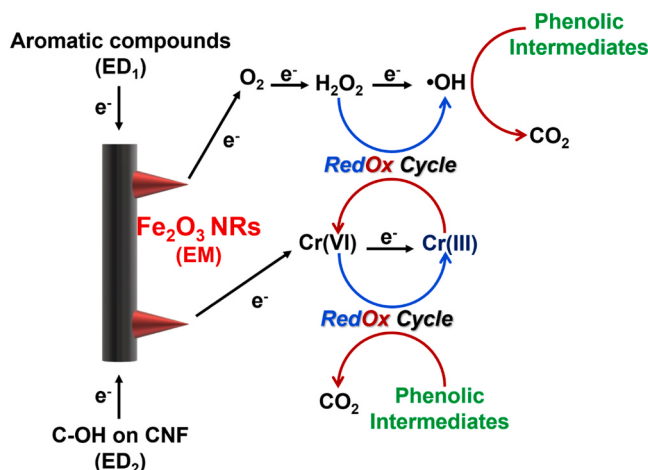
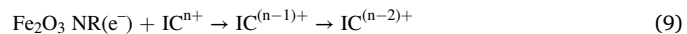
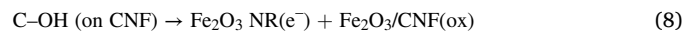
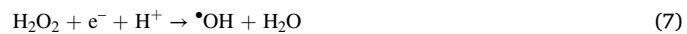


Fig. 8. Repetitive cycles of the simultaneous removal of (a) 4-CP oxidation and (b) Cr(VI) reduction. The SEM images of $\text{Fe}_2\text{O}_3/\text{CNF}$ (c) before and (d) after the 10th cycle of the simultaneous removal reactions. $[\text{Fe}_2\text{O}_3/\text{CNF}] = 2 \text{ g L}^{-1}$, $[4\text{-CP}]_0 = 20 \mu\text{M}$, and $[\text{Cr(VI)}]_0 = 40 \mu\text{M}$. Each reaction cycle was 6 h.



Scheme 1. Proposed mechanism of simultaneous redox conversions occurring on $\text{Fe}_2\text{O}_3/\text{CNF}$ through cascaded electron transfer path between aromatic compound and hexavalent chromium (ED: electron donor, EM: electron transfer mediator).

AC/IC conversion may serve as an additional oxidant or reductant. For example, low valent of chromium (e.g., Cr(III), Cr(IV), and Cr(V)) generated from Cr(VI) reduction may activate *in-situ* H_2O_2 to generate additional $\bullet\text{OH}$ (reaction 3), while phenolic oxidation intermediates may reduce Cr(VI) directly (reaction 1). Overall, $\text{Fe}_2\text{O}_3/\text{CNF}$ serves as a novel bifunctional Fenton-like catalyst that generates *in-situ* H_2O_2 spontaneously and facilitates the cascade electron transfer from AC to IC with achieving the simultaneous oxidative and reductive transformation of contaminants in ambient aerated solution.



3.5. Continuous flow reactor with $\text{Fe}_2\text{O}_3/\text{CNF}$ filter loaded

We applied the reactivity of $\text{Fe}_2\text{O}_3/\text{CNF}$ nanocomposite to the development of a reactive filter for water treatment. A flow reactor-based purification system was designed and evaluated for the simultaneous removal of organic and inorganic contaminants as shown in Fig. 9. The flowing reactor cell was set up to continuously inject a solution containing dual substrates (i.e., 4-CP||CrO₄²⁻, AP||SeO₃²⁻, BA||BrO₃) and flow through a reactive $\text{Fe}_2\text{O}_3/\text{CNF}$ filter (or bare CNF as a control) (see Fig. 9a and b). The removal efficiencies of the dual substrates were compared between the bare CNF and $\text{Fe}_2\text{O}_3/\text{CNF}$ systems as shown in Fig. 9c. The result indicates that only $\text{Fe}_2\text{O}_3/\text{CNF}$ exhibited outstanding performance as a reactive filter under the flowing condition, while bare CNF showed negligible activity. This highlights the potential of $\text{Fe}_2\text{O}_3/\text{CNF}$ as a water-treatment reactive filter that works for simultaneous redox conversions under ambient conditions without additional energy input and chemical reagents.

4. Conclusions

Conventional advanced oxidation processes (AOPs) and advanced reduction processes (ARPs) are carried out through the generation of potent oxidants and reductants, respectively, to remove or mineralize a

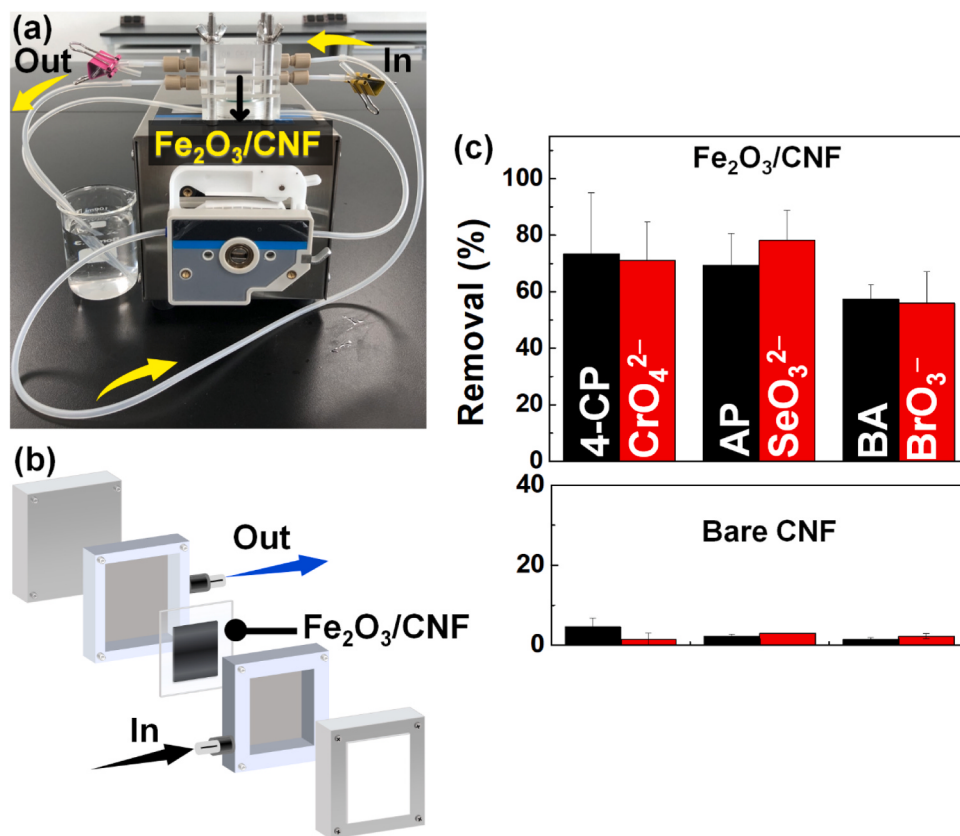


Fig. 9. (a) Photo image of the continuous-flow reactor setup for aqueous contaminants removal by Fe₂O₃/CNF filter inserted in a flow reactor cell. Fe₂O₃/CNF functions as a reactive filter to purify contaminated solution. The contaminated solution is circulated through the Fe₂O₃/CNF flow reactor by a peristaltic pump. (b) Schematic illustration of the Fe₂O₃/CNF filter inserted in a flow reactor cell. (c) Comparisons of the removal of various aqueous contaminant couples on bare CNF and Fe₂O₃/CNF filter under flowing condition for 24 h. Working size of Fe₂O₃/CNF = 2 x 2 cm², aqueous contaminants solution volume = 100 mL, [4-CP, AP, and BA]₀ = 10 μ M, [CrO₄²⁻, SeO₃²⁻, and BrO₃⁻]₀ = 20 μ M, and flow rate = 6.3 mL min⁻¹.

wide range of aqueous contaminants. However, the need for eco-friendly and low-cost materials, external energy input (e.g., electricity, photon), and chemical reagents (e.g., H₂O₂, O₃, persulfates) present significant challenges for the widespread use of these technologies. Most of the AOPs and ARPs are effective only for the removal of oxidizable and reducible contaminants, respectively, and leave the reducible and oxidizable contaminants largely intact, respectively. Therefore, there is a critical need to develop an advanced remediation system that can convert both oxidizable and reducible contaminants simultaneously. In this study, we propose a heterojunction nanocomposite Fe₂O₃/CNF as a bifunctional Fenton-like catalyst, which is composed of earth-abundant elements only and converts oxidizable and reducible contaminants simultaneously under ambient aerated conditions along with *in-situ* generation of H₂O₂. Fe₂O₃ or CNF alone or their physical mixture does not exhibit any reactivity. Fe₂O₃/CNF has several key advantages, including no requirement for harmful chemical reagents, no need for external energy input, no need for catalyst recovery, and an environmentally benign material of low cost. Furthermore, Fe₂O₃/CNF can initiate simultaneous and synergistic environmental redox conversions for a variety of aqueous contaminants, including aromatic compounds and reducible inorganic contaminants. The oxygen-containing functional group (C-OH) on the CNF surface serves as an electron donor to initiate the reductive transformation of the inorganic contaminants, while Fe₂O₃ sites can facilitate O₂ reduction for ROS generation. *In-situ* oxidants and reductants are generated during the overall redox conversions, which further facilitate the conversions. However, the overall redox reaction rates are relatively slow and may not be practical for removing high concentrations of aqueous contaminants. Therefore, it can be more effectively employed as a reactive filter material capable of

treating low-level contaminants under ambient aerated conditions. For instance, it can be utilized as a *point-of-use* device installed on the inner surface of a water container, whether for industrial or home use.

CRediT authorship contribution statement

Chuhyung Kim: Investigation, Conceptualization, Methodology, Formal analysis, Writing – original draft & editing, **Soonhyun Kim:** Investigation, Conceptualization, **Yiseul Park:** Conceptualization, Supervision, Writing – review & editing, **Funding acquisition, Wonyong Choi:** Conceptualization, Supervision, Writing – review & editing, **Funding acquisition.**

Declaration of Competing Interest

The authors declare that they have no known competing financial interests or personal relationships that could have appeared to influence the work reported in this paper.

Data availability

The data that has been used is confidential.

Acknowledgment

This work was supported by the Korean government (MSIT) through the National Research Foundation of Korea (NRF): Leading Researcher program (NRF-2020R1A3B2079953) and the NRF grant (2020R1C1C1010897). Assistance with the experiment from Dr.

Wonjung Choi is appreciated.

Appendix A. Supporting information

Supplementary data associated with this article can be found in the online version at [doi:10.1016/j.apcatb.2023.123287](https://doi.org/10.1016/j.apcatb.2023.123287).

References

- [1] H.J.H. Fenton, Oxidation of tartaric acid in presence of Iron, *J. Chem. Soc., Trans.* 65 (1894) 899–910.
- [2] H.-M. Feng, J.-C. Zheng, N.-Y. Lei, L. Yu, K.H.-K. Kong, H.-Q. Yu, T.-C. Lau, M.H. W. Lam, Photoassisted fenton degradation of polystyrene, *Environ. Sci. Technol.* 45 (2011) 744–750.
- [3] L. Mu, M. Wang, F. Jiang, Q. Gao, M. Zhang, Z. Xiong, Y. Li, R. Shen, J. Hu, G. Wu, Boosting Photo-Fenton reactions by amidoxime chelated ferrous iron (Fe(III)) catalyst for highly efficient pollutant control, *Appl. Catal. B: Environ.* 298 (2021) 120574.
- [4] S. Zheng, H. Chen, X. Tong, Z. Wang, J.C. Crittenden, M. Huang, Integration of a Photo-Fenton Reaction and a Membrane Filtration using CS/PAN@FeOOH/g-C₃N₄ Electrospun Nanofibers: Synthesis, Characterization, Self-cleaning Performance and Mechanism, *Appl. Catal. B: Environ.* 281 (2021) 119519.
- [5] H.-C. Li, X.-y. Ji, X.-Q. Pan, C. Liu, W.-J. Liu, Ionothermal Carbonization of Biomass to Construct Fe, N-Doped Biochar with Prominent Activity and Recyclability as Cathodic Catalysts in Heterogeneous Electro-Fenton, *ACS EST Engg* 1 (2021) 21–31.
- [6] G. Gao, Q. Zhang, Z. Hao, C.D. Vecitis, Carbon nanotube membrane stack for flow-through sequential regenerative electro-fenton, *Environ. Sci. Technol.* 49 (2015) 2375–2383.
- [7] Y. Liu, S. Chen, X. Quan, H. Yu, H. Zhao, Y. Zhang, Efficient mineralization of perfluorooctanoate by electro-fenton with H₂O₂ electro-generated on hierarchically porous carbon, *Environ. Sci. Technol.* 49 (2015) 13528–13533.
- [8] M. Liu, Z. Feng, X. Luan, W. Chu, H. Zhao, G. Zhao, Accelerated Fe²⁺ regeneration in an effective electro-fenton process by boosting internal electron transfer to a nitrogen-conjugated Fe(III) complex, *Environ. Sci. Technol.* 55 (2021) 6042–6051.
- [9] A. Xu, E. Brillas, W. Han, L. Wang, I. Sirés, On the positive effect of UVC light during the removal of benzothiazoles by photoelectro-Fenton with UVA light, *Appl. Catal. B: Environ.* 259 (2019), 118127.
- [10] F.C. Moreira, S. Garcia-Segura, V.J.P. Vilar, R.A.R. Boaventura, E. Brillas, Decolorization and mineralization of Sunset Yellow FCF azo dye by anodic oxidation, electro-Fenton, UVA photoelectro-Fenton and solar photoelectro-Fenton processes, *Appl. Catal. B: Environ.* 142–143 (2013) 877–890.
- [11] A. Wang, J. Qu, H. Liu, J. Ru, Mineralization of an azo dye Acid Red 14 by photoelectro-Fenton process using an activated carbon fiber cathode, *Appl. Catal. B: Environ.* 84 (2008) 393–399.
- [12] B. Zhang, X. Li, Y. Ma, T. Jiang, Y. Zhu, H. Ren, Visible-light photoelectrocatalysis/H₂O₂ synergistic degradation of organic pollutants by a magnetic Fe₃O₄@SiO₂/mesoporous TiO₂ catalyst-loaded photoelectrode, *RSC Adv.* 12 (2022) 30577–30587.
- [13] Z. Wang, S. Xu, J. Cai, J. Ma, G. Zhao, Perspective on photoelectrocatalytic removal of refractory organic pollutants in water systems, *ACS EST Engg* 2 (2022) 1001–1014.
- [14] M. Jain, M. Yadav, T. Kohout, M. Lahtinen, V. Kumar, G. Sillanpää, Development of iron oxide/activated carbon nanoparticle composite for the removal of Cr(VI), Cu (II) and Cd(II) ions from aqueous solution, *Water Resour. Ind.* 20 (2018) 54–74.
- [15] M. Bhaumik, A. Maity, V.V. Srinivasu, M.S. Onyango, Enhanced removal of Cr(VI) from aqueous solution using polypyrrole/Fe₃O₄ magnetic nanocomposite, *J. Hazard. Mater.* 190 (2011) 381–390.
- [16] Y. Cui, H. He, J.D. Atkinson, Iron/Carbon Composites for Cr(VI) Removal Prepared from Harmful Algal Bloom Biomass via Metal Bioaccumulation or Biosorption, *ACS Sustain. Chem. Eng.* 7 (2019) 1279–1288.
- [17] W. Jiang, Q. Cai, W. Xu, M. Yang, Y. Cai, D.D. Dionysiou, K.E. O'Shea, Cr(VI) adsorption and reduction by humic acid coated on magnetite, *Environ. Sci. Technol.* 48 (2014) 8078–8085.
- [18] Y. Zou, X. Wang, A. Khan, P. Wang, Y. Liu, A. Alsaedi, T. Hayat, X. Wang, Environmental remediation and application of nanoscale zero valent iron and its composites for the removal of heavy metal ions: a review, *Environ. Sci. Technol.* 50 (2016) 7290–7304.
- [19] M.M. Tarekegn, A.M. Hiruy, A.H. Dekebo, Nano zero valent iron (nZVI) particles for the removal of heavy metals (Cd²⁺, Cu²⁺ and Pb²⁺) from aqueous solutions, *RSC Adv.* 11 (2021) 18539–18551.
- [20] M. Liao, X. Wang, S. Cao, M. Li, X. Peng, L. Zhang, Oxalate modification dramatically promoted Cr(VI) removal with zero-valent iron, *ACS EST Water* 1 (2021) 2109–2118.
- [21] L. Gong, L. Zhang, Oxyanion-modified zero valent iron with excellent pollutant removal performance, *Chem. Commun.* 59 (2023) 2081–2089.
- [22] M. Li, Y. Mu, H. Shang, C. Mao, S. Cao, Z. Ai, L. Zhang, Phosphate modification enables high efficiency and electron selectivity of nZVI toward Cr(VI) removal, *Appl. Catal. B: Environ.* 263 (2020), 118364.
- [23] X. Lv, J. Xu, G. Jiang, J. Tang, X. Xu, Highly active nanoscale zero-valent iron (nZVI)-Fe₃O₄ nanocomposites for the removal of chromium(VI) from aqueous solutions, *J. Colloid Interface Sci.* 369 (2012) 460–469.
- [24] Y. Mu, Z. Ai, L. Zhang, F. Song, Insight into Core–Shell Dependent Anoxic Cr(VI) Removal with Fe@Fe₂O₃ Nanowires: Indispensable Role of Surface Bound Fe(II), *ACS Appl. Mater. Interfaces* 7 (2015) 1997–2005.
- [25] Y. Li, W. Cheng, G. Sheng, J. Li, H. Dong, Y. Chen, L. Zhu, Synergetic effect of a pillared bentonite support on SE(VI) removal by nanoscale zero valent iron, *Appl. Catal. B: Environ.* 174–175 (2015) 329–335.
- [26] D. Zhong, Y. Zhang, i Wang, J. Chen, Y. Jiang, D.C.W. Tsang, Z. Zhao, S. Ren, Z. Liu, J.C. Crittenden, Mechanistic insights into adsorption and reduction of hexavalent chromium from water using magnetic biochar composite: Key roles of Fe₃O₄ and persistent free radicals, *Environ. Pollut.* 243 (2018) 1302–1309.
- [27] L. Qian, Y. Chen, D. Ouyang, W. Zhang, L. Han, J. Yan, P. Kavipil, M. Chen, Field demonstration of enhanced removal of chlorinated solvents in groundwater using biochar-supported nanoscale zero-valent iron, *Sci. Total Environ.* 698 (2020), 134215.
- [28] Y. Sun, I.K.M. Yu, D.C.W. Tsang, X. Cao, D. Lin, L. Wang, N.J.D. Graham, D. S. Alessi, M. Komárek, Y.S. Oki, Y. Feng, X.-D. Li, Multifunctional iron-biochar composites for the removal of potentially toxic elements, inherent cations, and hetero-chloride from hydraulic fracturing wastewater, *Environ. Int.* 124 (2019) 521–532.
- [29] C. Kim, J. Lim, S. Kim, Y. Park, W. Choi, Fe₂O₃ nanorods on carbon nanofibers induce spontaneous reductive transformation of inorganic contaminants in ambient aerated water, *Chem. Eng. J.* 429 (2021), 132108.
- [30] Y. Park, C. Kim, M. Kim, S. Kim, W. Choi, Ambient-temperature catalytic degradation of aromatic compounds on iron oxide nanorods supported on carbon nanofiber sheet, *Appl. Catal. B: Environ.* 259 (2019), 118066.
- [31] Y. Park, M. Oh, J.S. Park, S.-H. Baek, M. Kim, S. Kim, J.H. Kim, Electrochemically deposited Fe₂O₃ nanorods on carbon nanofibers for free-standing anodes of lithium-ion batteries, *Carbon* 94 (2015) 9–17.
- [32] T.H. Jeon, G.-h Moon, H. Park, W. Choi, Ultra-efficient and durable photoelectrochemical water oxidation using elaborately designed hematite nanorod arrays, *Nano Energy* 39 (2017) 211–218.
- [33] Y.V. Nancharaiah, M. Sarvajith, P.N.L. Lens, Selenite reduction and ammoniacal nitrogen removal in an aerobic granular sludge sequencing batch reactor, *Wat. Res.* 131 (2018) 131–141.
- [34] E.-T. Yun, G.-h. Moon, H. Lee, T.H. Jeon, C. Lee, W. Choi, J. Lee, Oxidation of organic pollutants by peroxymonosulfate activated with low-temperature-modified nanodiamonds: Understanding the reaction kinetics and mechanism, *Appl. Catal. B: Environ.* 237 (2018) 432–441.
- [35] T.H. Jeon, H. Kim, H.-i Kim, W. Choi, Highly durable photoelectrochemical H₂O₂ production via dual photoanode and cathode processes under solar simulating and external bias-free conditions, *Energy Environ. Sci.* 13 (2020) 1730–1742.
- [36] C.C. Luhrs, M. Moberg, A. Maxson, L. Brewer, S. Menon, IF-WS2/nanostructured carbon hybrids generation and their characterization, *Inorganics* 2 (2014) 211–232.
- [37] L. He, A. Karumuri, S.M. Mukhopadhyay, Wettability tailoring of nanotube carpets: morphology-chemistry synergy for hydrophobic–hydrophilic cycling, *RSC Adv.* 7 (2017) 25265–25275.
- [38] S.-S. Li, W.-J. Li, T.-J. Jiang, Z.-G. Liu, X. Chen, H.-P. Cong, J.-H. Liu, Y.-Y. Huang, L.-N. Li, X.-J. Huang, Iron oxide with different crystal phases (α - and γ -Fe₂O₃) in electroanalysis and ultrasensitive and selective detection of Lead(II): An advancing approach using XPS and EXAFS, *Anal. Chem.* 88 (2016) 906–914.
- [39] A.P. Grosvenor, B.A. Kobe, N.S. McIntyre, Studies of the oxidation of iron by water vapour using X-ray photoelectron spectroscopy and QUASESTTM, *Surf. Sci.* 572 (2004) 217–227.
- [40] A.D. Bokare, W. Choi, Advaced oxidation process based on the Cr(III)/Cr(VI) redox cycle, *Environ. Sci. Technol.* 45 (2011) 9332–9338.
- [41] A.D. Bokare, W. Choi, Chromate-induced activation of hydrogen peroxide for oxidative degradation of aqueous organic pollutants, *Environ. Sci. Technol.* 44 (2010) 7232–7237.
- [42] D.-h Kim, D. Lee, D. Monllor-Satoca, K. Kim, W. Lee, W. Choi, Homogeneous photocatalytic Fe³⁺/Fe²⁺ redox cycle for simultaneous Cr(VI) reduction and organic pollutant oxidation: Roles of hydroxyl radical and degradation intermediates, *J. Hazard. Mater.* 372 (2019) 121–128.
- [43] Y. Choi, M.S. Koo, A.D. Bokare, D.-h Kim, D.W. Bahnemann, W. Choi, Sequential process combination of photocatalytic oxidation and dark reduction for the removal of organic pollutants and Cr(VI) using Ag/TiO₂, *Environ. Sci. Technol.* 51 (2017) 3973–3981.
- [44] M.S. Koo, K. Cho, J. Yoon, W. Choi, Photoelectrochemical degradation of organic compounds coupled with molecular hydrogen generation using electrochromic TiO₂ nanotube arrays, *Environ. Sci. Technol.* 51 (2017) 6590–6598.
- [45] Y. Zhang, X. Lin, Q. Zhou, X. Luo, Fluoride adsorption from aqueous solution by magnetic core-shell Fe₃O₄@alginate-La particles fabricated via electro-coextrusion, *Appl. Surf. Sci.* 389 (2016) 34–45.
- [46] Y.-H. Huang, Y.-J. Shih, Chia-Chi Chang, Adsorption of fluoride by waste iron oxide: the effects of solution pH, major coexisting anions, and adsorbent calcination temperature, *J. Hazard. Mater.* 186 (2011) 1355–1359.
- [47] M. Mohandoss, S.S. Gupta, A. Nelleri, T. Pradeep, S.M. Maliekal, Solar mediated reduction of graphene oxide, *RSC Adv.* 7 (2017) 957–963.
- [48] L.Y. Jun, N.M. Mubarak, L.S. Yon, C.H. Bing, M. Khalid, P. Jagadish, E.C. Abdullah, Immobilization of peroxidase on functionalized MWCNTs-buckypaper/polyvinyl alcohol nanocomposite membrane, *Sci. Rep.* 9 (2019) 2215.
- [49] J. Wang, C. Liu, B. Xiao, N. Cheng, A. Riese, M.N. Banis, X. Sun, Efficient oxygen reduction electrocatalyst from graphene by simultaneously generating pores and nitrogen doped active sites, *ChemElectroChem* 4 (2017) 296–303.
- [50] S.A. Chernyak, A.S. Ivanov, K.I. Maslakov, A.V. Egorov, Z. Shen, S.S. Savilov, V. V. Luninab, Oxidation, defunctionalization and catalyst life cycle of carbon

nanotubes: a Raman spectroscopy view, *Phys. Chem. Chem. Phys.* 19 (2017) 2276–2285.

[51] S.-H. Yu, D.E. Conte, S. Baek, D.-C. Lee, S.-K. Park, K.J. Lee, Y. Piao, Y.-E. Sung, N. Pinna, Structure-properties relationship in iron oxide-reduced graphene oxide nanostructures for Li-ion batteries, *Adv. Funct. Mat.* 23 (2013) 4293–4305.

[52] S. Trudel, E.D. Crozier, R.A. Gordon, P.S. Budnik, R.H. Hill, X-ray absorption fine structure study of amorphous metal oxide thin films prepared by photochemical metalorganic deposition, *J. Sol. State Chem.* 184 (2011) 1025–1035.